

DMS-MaPseq for genome-wide or targeted RNA structure probing *in vivo*

Meghan Zubradt¹, Paromita Gupta², Sitara Persad², Alan M Lambowitz³, Jonathan S Weissman¹ & Silvi Rouskin²

Coupling of structure-specific *in vivo* chemical modification to next-generation sequencing is transforming RNA secondary structure studies in living cells. The dominant strategy for detecting *in vivo* chemical modifications uses reverse transcriptase truncation products, which introduce biases and necessitate population-average assessments of RNA structure. Here we present dimethyl sulfate (DMS) mutational profiling with sequencing (DMS-MaPseq), which encodes DMS modifications as mismatches using a thermostable group II intron reverse transcriptase. DMS-MaPseq yields a high signal-to-noise ratio, can report multiple structural features per molecule, and allows both genome-wide studies and focused *in vivo* investigations of even low-abundance RNAs. We apply DMS-MaPseq for the first analysis of RNA structure within an animal tissue and to identify a functional structure involved in noncanonical translation initiation. Additionally, we use DMS-MaPseq to compare the *in vivo* structure of pre-mRNAs with their mature isoforms. These applications illustrate DMS-MaPseq's capacity to dramatically expand *in vivo* analysis of RNA structure.

RNA is a functionally diverse molecule that both carries genetic information and directly conducts biological processes through its ability to fold into complex secondary and tertiary structures¹. The discovery of functional RNA structures depends critically on accurate, targeted, and accessible RNA structure determination methods, particularly *in vivo*. Sequence information alone is generally not sufficient for prediction of RNA structure, but by combining sequence information with experimental structure data at single-nucleotide resolution, one can often obtain an accurate assessment of RNA folding status and discover novel RNA structures^{2–4}.

Existing high-resolution techniques to measure RNA secondary structure are based on structure-specific chemical modification. DMS has emerged as one of the pre-eminent choices for this application. DMS rapidly and specifically modifies unpaired adenines and cytosines *in vivo* at their Watson–Crick base-pairing positions⁵. Selective 2'-hydroxyl acylation analyzed by primer extension (SHAPE) chemicals are another powerful option for

chemical RNA structure probing. Because of their distinct mechanisms of modification, DMS and SHAPE report on different and complementary aspects of RNA structure^{6,7}. In early efforts, chemical lesions from either SHAPE or DMS were detected when the reverse transcriptase (RT) enzyme terminated cDNA synthesis upon reaching a modified nucleotide. We and others have coupled the chemical probing of RNA structure to next-generation sequencing (Fig. 1), allowing for experimental analysis of RNA structure on a global scale *in vitro* or *in vivo*^{4,8–11} (see refs. 12 and 13 for reviews of sequencing-coupled RNA structure techniques). Globally, these experiments have revealed substantial differences in RNA structure *in vivo* versus *in vitro*, underscoring the importance of examining RNA structure in its native cellular environment^{4,10}.

Despite important contributions to RNA structure discovery, truncation-based approaches using either DMS or SHAPE have intrinsic limitations that render them unsuitable to address certain biological questions, such as the heterogeneity of RNA structures *in vivo*. We sought to develop an *in vivo* and genome-wide approach that would overcome existing limitations in truncation strategies by encoding DMS lesions as mutations instead of as cDNA truncations, as has been recently described for individual or highly abundant RNA targets^{7,14–16}. Such mutational profiling (MaP) approaches confer several advantages. These advantages include the resolution of enzymatic biases proximal to the information-encoding nucleotide and (most importantly) the analysis of multiple chemical modification sites per molecule, which opens up the possibility of distinguishing heterogeneous RNA structure subpopulations from one another *in vivo*. In truncation approaches, only a single site of chemical modification can be observed per RNA molecule; thus, the structure signal corresponds to a population average. Additionally, low-abundance RNAs are not conducive to truncation-based RNA structure probing. Specifically, they are poorly sequenced on a genome-wide scale, and input requirements for available low-throughput methods often necessitate *in vitro* transcription before structure profiling^{6,14,15,17}. We reasoned that an *in vivo* MaP approach would make it possible to perform targeted amplification of low-abundance RNA species while retaining a record of the modification sites.

¹Department of Cellular and Molecular Pharmacology, California Institute of Quantitative Biology, Center for RNA Systems Biology, Howard Hughes Medical Institute, University of California, San Francisco, San Francisco, California, USA. ²Whitehead Institute for Biomedical Research, Cambridge, Massachusetts, USA. ³Institute for Cellular and Molecular Biology, Department of Molecular Biosciences, University of Texas at Austin, Austin, Texas, USA. Correspondence should be addressed to J.S.W. (jonathan.weissman@ucsf.edu) or S.R. (srouskin@wi.mit.edu).

Here we describe DMS-MaPseq, an RNA structure probing strategy that takes advantage of a high-fidelity and processive thermostable group II reverse transcriptase (TGIRT) enzyme. We apply this technique globally *in vivo* and for selected RNA species, including low-abundance RNA targets in yeast and human cells, producing the high signal and low background necessary for high data quality. We also highlight a simple RT-PCR approach for targeted amplification and demonstrate RNA experiments inaccessible by previous techniques such as the investigation of isoform-specific RNA structure and the discovery of a functional structure in the low-abundance human *FXR2* mRNA. DMS-MaPseq enables a far broader exploration of *in vivo* RNA structure and offers an accessible technical solution to address structure–function hypotheses for virtually any RNA, regardless of its abundance.

RESULTS

Development of genome-wide *in vivo* RNA structure probing with mutational profiling

For DMS-MaPseq, we treated cells with a high concentration of DMS to increase the number of modifications detected per fragment, modifying approximately 1 in 50 nucleotides. We compared data produced at this DMS concentration (5% v/v) to previously validated concentrations⁴, and we observed excellent correlation of the RNA structure signal both globally and for each nucleotide in the yeast 18S rRNA (Supplementary Fig. 1; $R = 0.94$ and $R = 0.98$, respectively). For applications that aim to use even higher DMS levels, it will be important to do a similar analysis to evaluate whether RNA structures are perturbed with increasing DMS concentrations. After DMS treatment and total RNA extraction, random fragmentation with Zn^{2+} , and the removal of ribosomal RNA, we did a broad size selection, ligated a 3' adaptor, and reverse transcribed under conditions in which chemically modified bases were encoded as mutations in the cDNA (Fig. 1). Consequently, multiple modifications can be observed on a single cDNA fragment, providing an essential framework for future applications of single-molecule RNA structure determination.

The accuracy of DMS-MaPseq depends critically on reverse transcription conditions that optimize the detection of DMS modifications while retaining high fidelity and processivity during cDNA synthesis. The TGIRT enzyme was recently adapted with these latter priorities in mind and notably produces mismatches at endogenous m^1A and m^3C tRNA residues—the exact methylation profiles of a DMS modification^{18,19}. Additionally, Superscript II with Mn^{2+} buffer (SSII- Mn^{2+}) has been used for the

mutational read through of DMS and SHAPE modifications for abundant individual RNA species^{14–16}. To compare the suitability of these two enzymes for our *in vivo* DMS-MaPseq approach, we prepared genome-wide yeast libraries with each. Encoding DMS modifications as mismatches inherently retains the single-nucleotide resolution of DMS while insertions or deletions (indels) suffer from positional ambiguity when aligned across a homopolymeric stretch. TGIRT does not produce a high number of indels (6%, Fig. 2a). However, we found that nearly a third of DMS-induced mutations from SSII- Mn^{2+} reverse transcription were insertions or deletions. Next, we used two endogenous m^1A modifications on the yeast 25S rRNA as internal controls for DMS lesion detection. The frequency of mismatches at these residues across TGIRT replicate experiments revealed m^1A detection at 85% and 48% average frequency, placing a lower bound on the fraction of these endogenous modifications. SSII- Mn^{2+} yielded average detection frequencies of only 53% and 1.4% at the same modified residues (Fig. 2b). This tendency of SSII- Mn^{2+} to under-report the DMS modification signal in a context-dependent manner could severely undermine data quality.

A valuable measure for the signal-to-noise ratio in DMS data is the enrichment of signal on adenines and cytosines⁴ (Supplementary Fig. 2a). When the same source of DMS-modified RNA was reverse transcribed using either TGIRT or SSII- Mn^{2+} , we observed a far greater fraction of mismatches on A–Cs using TGIRT (TGIRT, 93.5%; SSII- Mn^{2+} , 84%) (Fig. 2c). This high A–C signal in TGIRT data also exceeds that of our previously published DMS-seq strategy based on cDNA truncation, and there are notable differences in the relative contributions of A–Cs⁴. Analysis of the mismatch nucleotide bias in DMS-seq reveals that 54% of mismatches occur on cytosines in a DMS-dependent manner, suggesting that truncation at cytosines is not robust¹⁴ (Supplementary Fig. 2b,c). Notably, the signal on adenines is lower with SSII- Mn^{2+} than with the other techniques, which suggests an underlying failure of SSII- Mn^{2+} to robustly encode m^1A modifications consistent with the low signal detection on the endogenous rRNA residues.

Both TGIRT and SSII- Mn^{2+} produce excellent signal at unpaired A–C residues in the yeast *RPS28B* positive-control structure, but the SSII- Mn^{2+} data reveal high background signal on certain G–U residues, suggesting a propensity for nonrandom errors in cDNA synthesis. This higher background error for SSII- Mn^{2+} is also reflected in the genome-wide frequency of mutations and indels on matched untreated and DMS-treated RNA (Supplementary Fig. 2d), which is consistent with the historical use of Mn^{2+} buffer in deliberate mutagenesis during oligonucleotide

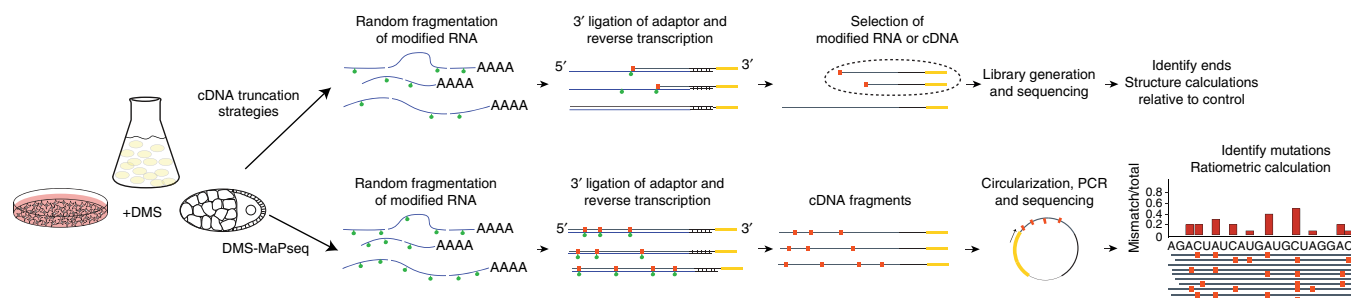


Figure 1 | Sequencing library generation for RNA structure probing techniques. Schematic of library preparation strategies for cDNA truncation approaches (top) and for DMS-MaPseq (bottom).

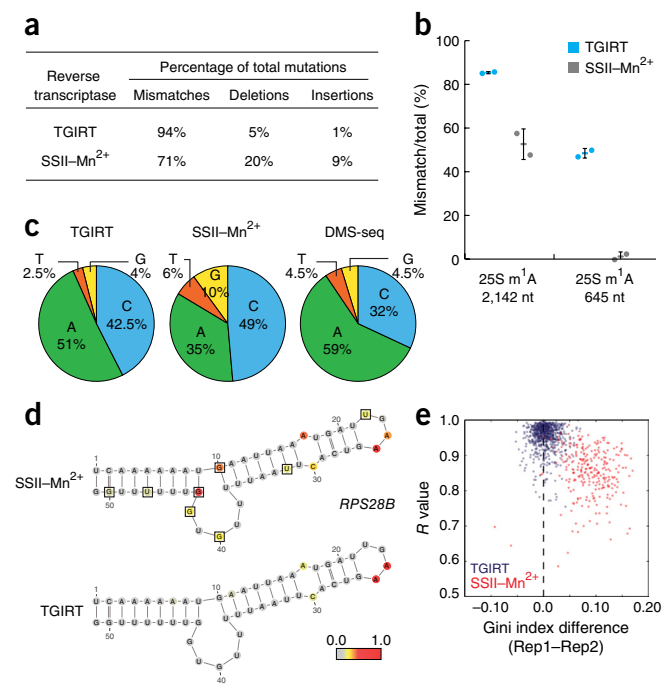


Figure 2 | TGIRT enzyme delivers higher signal and lower background for DMS-MaPseq. (a) Distribution of mutation type generated by SSII-Mn²⁺ or TGIRT reverse transcription from *in vivo* DMS-treated yeast mRNA. (b) Endogenous m¹A modifications in yeast 25S rRNA transcript reveal superior modification detection with TGIRT. Average percent modification (bar) detected at the position across two biological DMS-treated replicates (circles) with error bars representing s.d. from the average. (c) Nucleotide composition of mismatches from TGIRT or SSII-Mn²⁺ approaches. (d) Yeast *RPS28B* mRNA positive-control structure with nucleotides colored by DMS reactivity *in vivo*. Numbers represent the nucleotide position within the displayed region. Black boxes outline G–U bases with high background signal. DMS reactivity was calculated as the average ratiometric DMS signal per position across two biological replicates normalized to the highest number of reads in displayed region, which is set to 1.0. (e) Genome-wide DMS-MaPseq replicates (Rep1 and Rep2) compared by Pearson's *R* value and Gini index for yeast mRNA regions (requiring 15× coverage, resulting in 733 and 272 regions displayed for TGIRT and SSII-Mn²⁺, respectively).

synthesis²⁰. Other RNA structure methods have subtracted background signal on a nucleotide-by-nucleotide basis¹⁵; however, we see an increase in noise after applying a background correction to the *RPS28B* positive-control structure²¹ (Fig. 2d and Supplementary Fig. 3a–d). Global investigation reveals a poor correlation of background signal for both TGIRT and SSII-Mn²⁺ untreated replicates, suggesting that background signal is variable and stochastic (Supplementary Fig. 3e,f). Thus, a key advantage of DMS-MaPseq is the ratiometric nature of the data (i.e., in a population-level analysis, the rate of modification at each position is equal to the ratio of mutated reads to total reads; Fig. 1). Untreated or denatured DMS-MaPseq controls may still be useful in the discovery of endogenous mRNA modifications encoded during reverse transcription¹⁹, uncharacterized single-nucleotide polymorphisms, or as a negative control, but it is not a necessary component for single-nucleotide RNA structure calculations.

We used replicates to assess the reproducibility of the RNA structure signal across yeast transcriptome regions as measured by *r* value and the Gini index difference, an established RNA

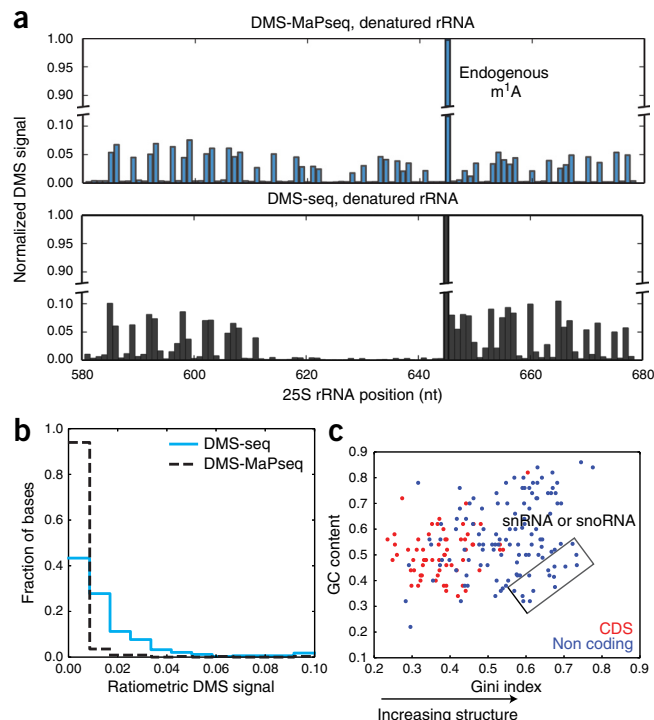


Figure 3 | Global analysis of *in vivo* DMS-MaPseq data. (a) Signal decay observed after endogenous m¹A modification at position 642 in the yeast 25S rRNA in DMS-seq but not in DMS-MaPseq. (b) Histogram of ratiometric reactivity for negative-control bases in the yeast 18S rRNA. The total number of negative-control bases is 338, characterized as bases known to be base paired. (c) Scatter plot of GC content versus Gini index in 50-nucleotide (nt) windows of deeply sequenced genes. Noncoding RNA regions include UTRs and all classes of mammalian noncoding RNAs. CDS regions are coding regions. A gray box is placed around small nuclear RNAs (snRNAs) and small nucleolar RNAs (snoRNAs). The total number of evaluated windows is 182. Pearson's correlation = 0.32; *P* value = 7.3×10^{-6} .

structure metric to assess the evenness of the data distribution⁴ (Fig. 2e). This analysis revealed a stronger reproducibility between data generated by TGIRT than by SSII-Mn²⁺, consistent with our observations of high background noise in the latter approach. Because of the high DMS signal and low background error observed across many quality control metrics, we chose the TGIRT enzyme for all further DMS-MaPseq experimentation and method development.

Global analysis of DMS-MaPseq data

When DMS lesions are detected by truncation, only the most 3' DMS modification on an RNA fragment will be detected. For this reason, DMS treatment conditions must be carefully titrated to avoid improper hit kinetics and 5' signal decay²². This effect is illustrated by the lack of DMS-seq signal immediately 5' of an endogenous m¹A residue in denatured yeast 25S rRNA (Fig. 3a). This drop off does not occur with DMS-MaPseq data, confirming that the TGIRT enzyme can encode multiple DMS lesions in a short sequence space. Additionally, negative-control bases in the yeast rRNA fall overwhelmingly into the lowest bin of reactivity in DMS-MaPseq data, confirming low background noise relative to previous DMS-seq data⁴ (Fig. 3b).

We also collected a genome-wide *in vivo* DMS-MaPseq data set from human embryonic kidney (HEK) 293T cells, and we

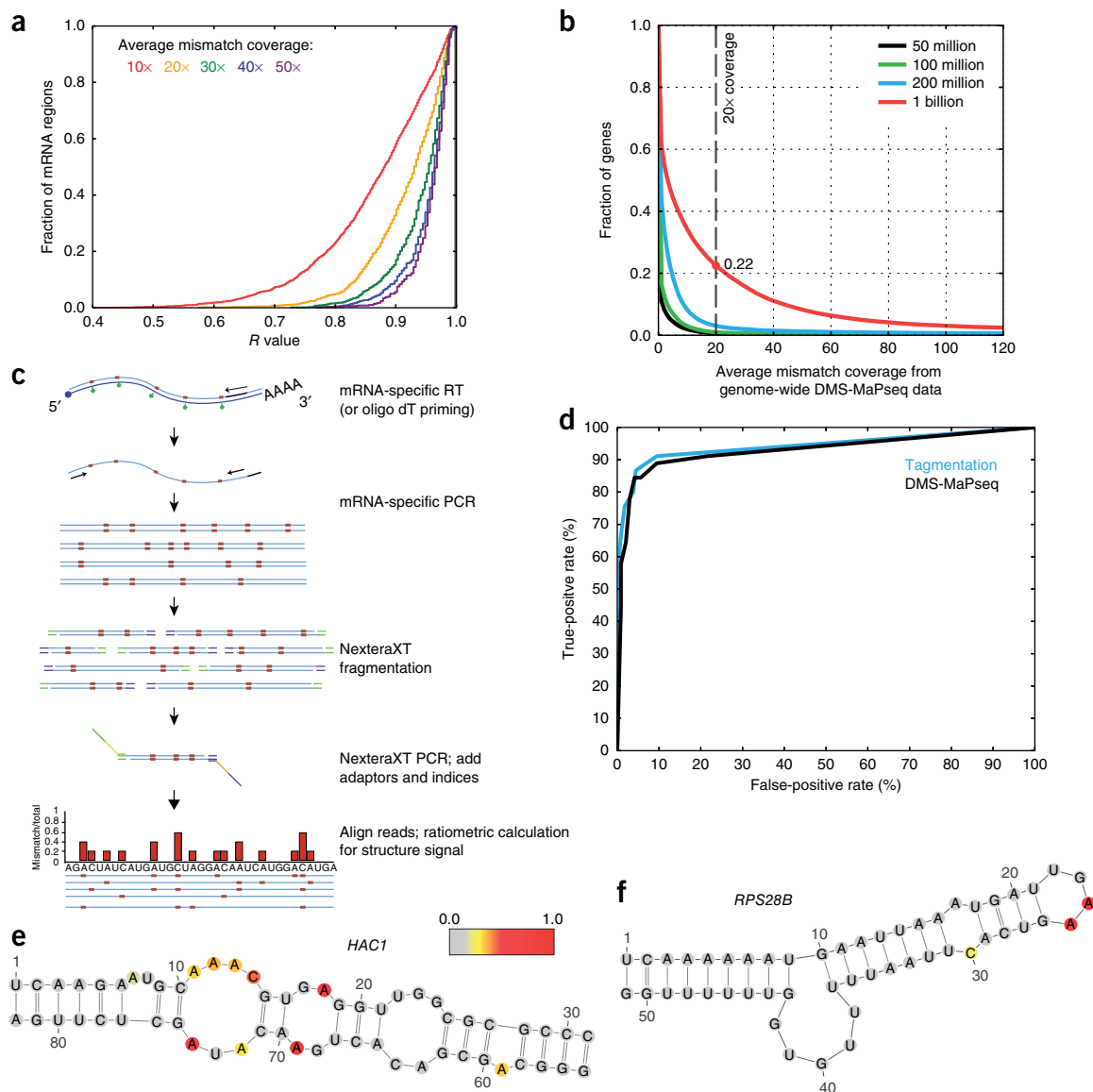


Figure 4 | DMS-MaPseq enables *in vivo* RNA structure probing for specific RNA targets. **(a)** Cumulative histogram of Pearson's R values between yeast mRNA regions in DMS-MaPseq replicates at varied depths of average mismatch coverage. **(b)** Fraction of genes exceeding the minimum average mismatch coverage of 20 \times in genome-wide human HEK 293T DMS-MaPseq data with varied sequencing depths. 0.006, 0.009, and 0.03 are the fraction of genes passing this threshold at 50, 100, and 200 million uniquely mapped reads, respectively. **(c)** Schematic for targeted RNA structure probing via target-specific RT-PCR and NexteraXT fragmentation. **(d)** ROC curve for DMS signal on yeast 18S rRNA using ratiometric data from target-specific fragmentation approach and from genome-wide DMS-MaPseq. **(e, f)** Yeast *HAC1* **(e)** and *RPS28B* **(f)** 3' UTR mRNA positive-control structures from target-specific priming with nucleotides colored by DMS reactivity *in vivo*. DMS reactivity calculated as the ratiometric DMS signal per position normalized to the highest number of reads in displayed region, which is set to 1.0.

confirmed the agreement of our data with the *XBPI* positive-control structure²³ (**Supplementary Fig. 4**). Often, a region of high GC content is considered a candidate region for RNA folding owing to the high stability of G–C pairings, so we investigated this relationship across human transcriptome regions, plotting GC content against the Gini index from DMS-MaPseq (**Fig. 3c**). A small correlation ($R = 0.32$) exists, but overall, coding regions have lower GC content, and their RNA appears less structured, as we demonstrated previously⁴. However, the lack of structure is more pronounced than expected by GC content alone, and noncoding RNA regions are more structured than coding DNA sequence (CDS) regions of comparable GC content. Interestingly,

the biggest outliers are small nucleolar RNAs (snoRNAs) and small nuclear RNAs (snRNAs), which have a low GC content but are highly structured.

DMS-MaPseq for specific or low-abundance RNA targets

Low-abundance mRNAs do not receive sufficient sequencing coverage in genome-wide experiments to enable robust conclusions about their structure. Plotting the cumulative r value distribution for mRNA regions between *in vivo* DMS-MaPseq replicates in yeast reveals that an average mismatch coverage depth of greater than 20 \times greatly improves data reproducibility (**Fig. 4a**). However, for genome-wide HEK 293T DMS-MaPseq data, only a limited

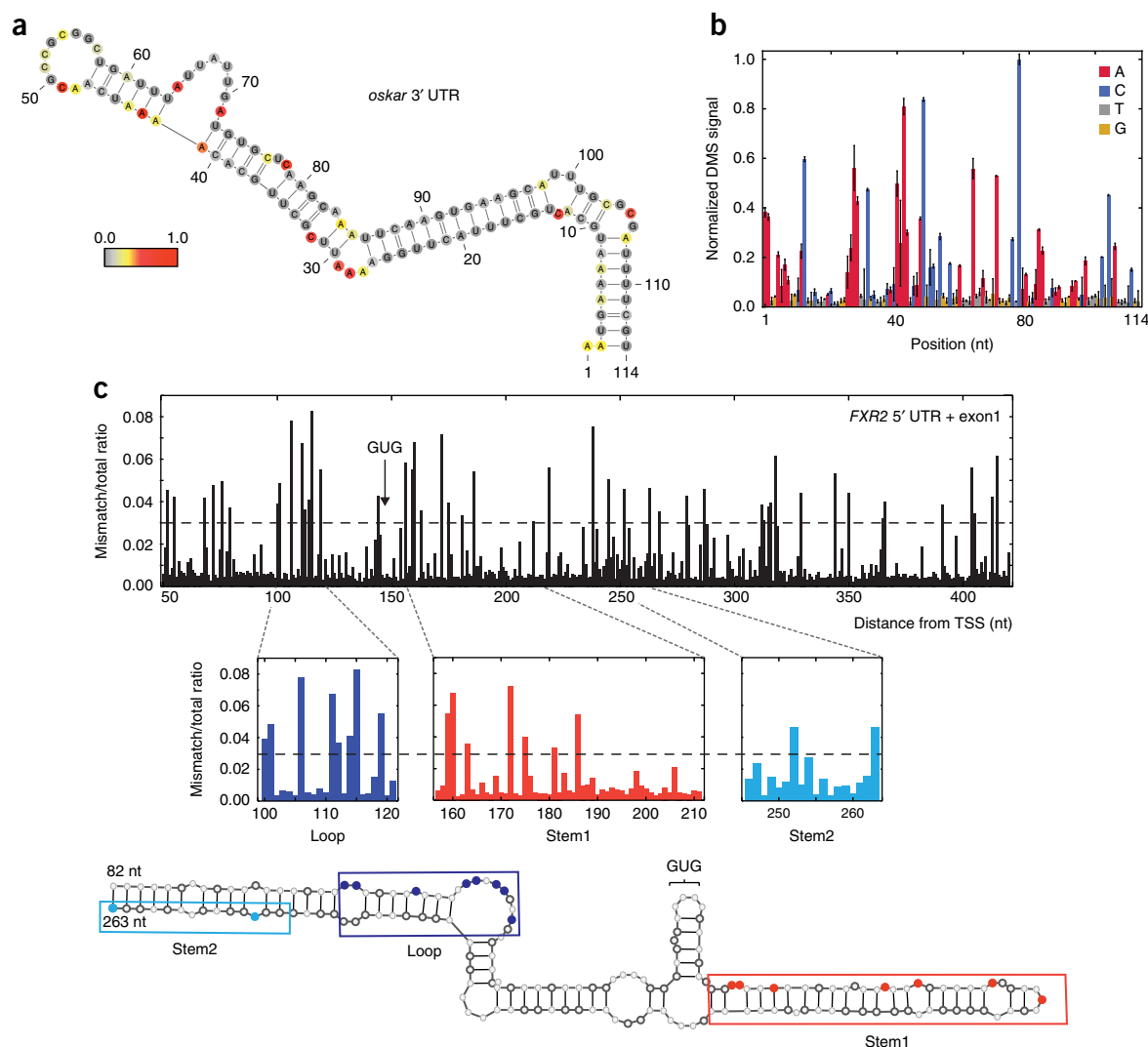


Figure 5 | Novel experimental applications for *in vivo* RNA structure probing. **(a)** *oskar* 3' UTR mRNA positive-control structure from target-specific priming with nucleotides colored by *in vivo* DMS reactivity in *D. melanogaster* ovaries. DMS reactivity calculated as the ratiometric DMS signal per position normalized to the highest number of reads in displayed region, which is set to 1.0. **(b)** *oskar* positive-control region from **a** shown with average normalized DMS-MaPseq values from two biological replicates, one at 5 min DMS treatment and one at 10 min. Error bars represent 1 s.d. **(c)** Ratiometric DMS-MaPseq from targeted amplification of the human *FXR2* 5' UTR and exon1 sequence. Nucleotides accessible to DMS are noted with a value >0.03, which is the threshold representing the best agreement with our model. Position 1 corresponds to chromosome XVII:7614897.

fraction of genes pass this 20× coverage threshold (Fig. 4b). Even when extrapolated to an exorbitant sequencing depth of 1 billion uniquely mapped reads, many human genes (78%) have insufficient coverage. To probe the *in vivo* structure of low-abundance mRNAs, we developed and validated a simple targeted RT-PCR implementation of DMS-MaPseq (Fig. 4c). Targeted DMS-MaPseq begins with the *in vivo* modification of RNA, followed by total RNA extraction, DNase treatment, and rRNA depletion. Then, we reverse-transcribe using the TGIRT enzyme and target-specific primers (primers can be used in combination to amplify multiple RNA species in a single reaction). Directly after cDNA synthesis, target-specific PCR primers amplify the RNA region of interest, and this is followed by NexteraXT tagmentation and sequencing.

To assess data quality from this targeted approach, we examined the structure signal for known RNA structures. We plotted a receiver operating characteristic (ROC) curve to assess the

concordance of 18S rRNA DMS-MaPseq data with the published yeast crystal structure model²⁴ and observed an excellent agreement with data from both our genome-wide and targeted approach (Fig. 4d and Supplementary Fig. 5a). We also assessed whether the targeted DMS-MaPseq data supported positive-control mRNA structure models, and we observed excellent agreement with the yeast *HAC1* and *RPS28B* structures^{21,25} (Fig. 4e,f) as well as with the human *XBP1* and *MSRB1* structures^{23,26} (Supplementary Fig. 5b–e). Finally, we observed no signal drop-off in our amplified regions until the primer-binding region, and we observed a low level of background signal (Supplementary Fig. 6).

To reduce PCR amplification biases for quantitative applications or low-input material, we also developed a variation of targeted DMS-MaPseq that tags each RNA molecule with a unique molecular index (UMI) on the RT primer (Supplementary Fig. 7a and Supplementary Table 1). Unique reads can then be isolated easily based on their specific UMI and DMS mutation profiles.

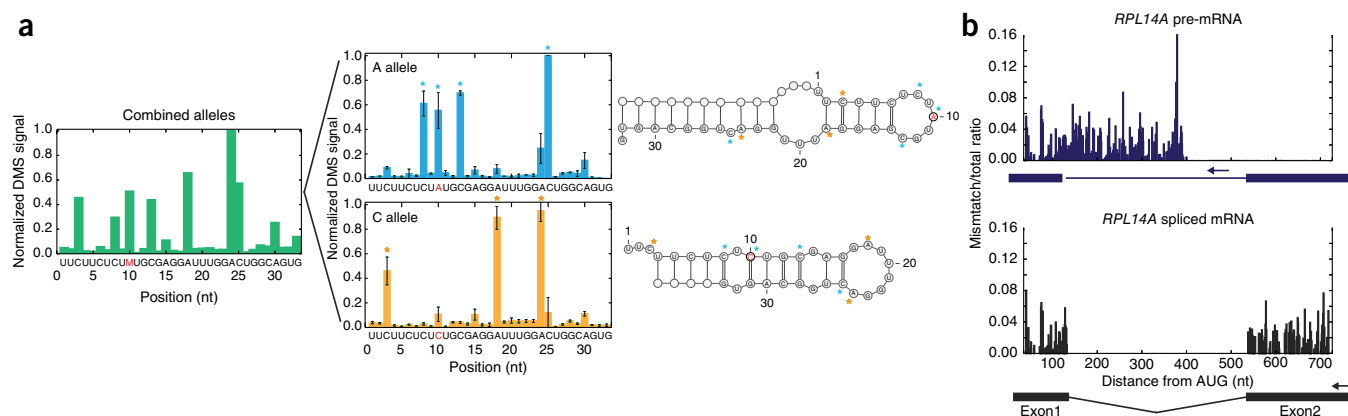


Figure 6 | Investigating RNA structure heterogeneity with DMS-MaPseq. **(a)** Regions of heterogeneous structure exhibit indistinguishable structure signals when combined but can be distinguished by DMS-MaPseq, which is illustrated by normalized DMS-MaPseq data derived from the human *MRPS21* ribosnitch A–C alleles. Allele-specific data represented as the mean of three technical replicates. Error bars represent 1 s.d.; stars mark A–C nucleotides with different pairing states between alleles. **(b)** Targeted DMS-MaPseq data specific for the yeast *RPL14A* pre-mRNA and spliced mRNA isoforms reveal minimal structure difference in the common exon1 sequence ($R = 0.88$). Ratiometric *in vivo* DMS-MaPseq data is plotted with isoform-specific RT primer locations noted with arrows.

The *SFT2* and *ASH1* yeast mRNAs are weakly expressed and host functional RNA structures in their 5' and 3' UTRs, respectively, serving as positive controls for DMS signal detection using a UMI. Indeed, both controls show DMS modification profiles consistent with the known secondary structure models^{4,27} (Supplementary Fig. 7b,c). Irrespective of their uniqueness, these data are in excellent agreement when processed, which suggests that a UMI may not be necessary for amplification of transcripts of comparable abundance. Given the limitations regarding the size of RNA region assayed with this UMI approach and the expense of longer sequencing reads, choosing between the targeted versions of DMS-MaPseq depends on the region size, target abundance, and quantitative demands of an experiment.

DMS-MaPseq for *Drosophila melanogaster* ovaries

With their dramatic developmental changes independent of transcription and mRNA degradation, *D. melanogaster* oocytes provide a premier system for studying mRNA localization and translational control. Many mRNAs are localized during oogenesis²⁸, and while these localization mechanisms are poorly understood globally, RNA structure has been shown to be involved^{29–31}. Here, we apply targeted DMS-MaPseq to *D. melanogaster* ovaries, which yields excellent structure data at two DMS treatment levels consistent with the *oskar* and *gurken* mRNA structures responsible for localization^{31,32} (Fig. 5a,b and Supplementary Fig. 8). This is the first example of RNA structure probing in an animal tissue and marks a key step forward in investigating the role of RNA structure in mRNA localization in this model system.

A highly structured region influences noncanonical translation initiation

We recently discovered that translation of the mammalian *FXR2* (Fragile X Mental Retardation, Autosomal Homolog 2) gene initiates predominantly at a GUG codon³³. On account of the extreme GC content (80%) of the first exon of *FXR2*, we hypothesized a stable RNA structure may contribute to the non-canonical initiation. We used *in vitro* DMS-MaPseq data to develop a secondary structure model with RNAfold³⁴. This revealed two highly stable putative structures flanking the GUG initiation codon (Fig. 5c,

Supplementary Fig. 9; free energy < –31 kcal/mol), with some ambiguity across certain regions depending on the thresholds used to impose folding constraints (see alternative structure model, Supplementary Fig. 10a). We mutated these putative *FXR2* structures to perturb the majority of base-pairing interactions in both models and tested their effects within a reporter construct, revealing a drop in protein levels upon mutating either structure (Supplementary Fig. 10b–d and Supplementary Table 2). Compensatory mutations, designed to optimize the restoration of our predicted RNA structures, restored eGFP levels and thus implicated the structure itself as a functional modulator of translation initiation for *FXR2*. In addition to the compensatory mutations, the *in vivo* structure signal supports this model (Supplementary Fig. 9c–e).

Structure probing of RNAs in multiple conformations

In the complex environment of the cell, the structure of an RNA molecule may vary based on its current state, such as maturation, translation, protein binding, and degradation. In the case of structural heterogeneity from a ribosnitch (i.e., a single-nucleotide polymorphism that yields a local RNA structure rearrangement), the interpretation of *in vitro* RNA folding status differs greatly when DMS-MaPseq data from the two human *MRPS21* ribosnitch alleles³⁵ are analyzed together or separately. Allele-specific analysis of the data reveals two distinct and mutually exclusive structures, which are not detectable from the combined allele analysis (Fig. 6a). This example illustrates the complexity of analyzing structurally heterogeneous regions and a simple resolution using DMS-MaPseq to separate specific RNA subpopulations by allele.

Of particular interest regarding structural heterogeneity are isoform-specific RNA structures. Structure differences have been proposed between pre-mRNAs and their mature translated counterparts, such as RNA structures that influence splice-site selection³⁶ or affect translation^{37,38}. We used intron- or exon-specific RT primers to separately amplify each isoform of two yeast ribosomal protein genes using targeted DMS-MaPseq. The RNA structure signal in the common exon1 sequence between the *RPL14A* and *RPL31B* pre-mRNAs and their respective mature counterparts reveals surprisingly little structure difference

between isoforms (Fig. 6b, Supplementary Figs. 11 and 12). These mRNAs are highly translated, but their exon1 structure is similar to that of the untranslated pre-mRNA, suggesting that local RNA structure rapidly refolds after translation. While we focus here on a limited number of messages, this approach broadly enables the analysis of different RNA isoforms.

DISCUSSION

Here we establish DMS-MaPseq as a robust and simple tool suitable for the quantitative analysis of RNA secondary structure *in vivo* by improving the inherent quality of the structure data, enabling qualitatively new types of structure to be gathered, and greatly expanding the repertoire of RNAs that can be analyzed. Future applications include *in vivo* single-molecule analyses of the co-occurrence of DMS modifications to identify heterogeneous RNA structure subpopulations (e.g., riboswitches³⁵) empirically. Additionally, DMS-MaPseq allows the selective amplification of RNA targets, including pre-mRNAs or differentially spliced isoforms. Together, these advances drastically expand the range of experimentally accessible RNA species for structural analysis, enabling a wide range of future studies. In theory, our *in vivo* MaP approach with TGIRT could also be used for SHAPE, which would be a valuable and complementary approach. However, the bulky nature of the best characterized and validated *in vivo* SHAPE chemical, NAI-N₃ (ref. 10), may prove challenging. Finally, DMS-MaPseq could be combined with the analysis of endogenous mRNA modifications, including the sequencing-based mapping of pseudouridines or m⁶A methylation^{39–42}. These endogenous modifications occur on only a subset of their RNA targets. Combined with the single-molecule aspects of DMS-MaPseq, it would be possible to evaluate how such endogenous RNA modification affects structure within a single experiment. It is the versatility of DMS-MaPseq that makes it a transformative tool for *in vivo* RNA structure probing, allowing for more comprehensive investigations into the biological relevance of RNA structures than ever before.

METHODS

Methods and any associated references are available in the [online version of the paper](#).

Accession codes. Raw and processed data are available at NCBI Gene Expression Omnibus, accession number [GSE84537](#).

Note: Any Supplementary Information and Source Data files are available in the online version of the paper.

ACKNOWLEDGMENTS

We thank A. Fields from UCSF for *FXR2* reporter plasmids; T. Norman, A. Fields, and J. Quinn for insightful discussions and comments on the manuscript; A. Jaeger (Whitehead Institute for Biomedical Research, Cambridge, Massachusetts, USA) for providing HEK 293T cells; and the Orr-Weaver lab at the Whitehead Institute for providing flies. We also thank Y. Chen, D. Bogdanoff, E. Chow, and J. Lund at the UCSF Center for Advanced Technology for sequencing assistance; J. Love and S. Levine in the Whitehead Core and MIT BioMicro Center for library preparation; and C. Reiger, M. DeVera, J. Kanter, and G. McCauley for administrative support. This research was supported by the CRSB (Center for RNA Systems Biology; grant P50 GM102706 to J.S.W.), the Howard Hughes Medical Institute (J.S.W.), the National Science Foundation grant 1144247 (M. Z.), and the Genentech Foundation (M.Z.). Research on TGIRTs and their modes of use was supported by NIH R01 grants GM37949 and GM37951 (A.M.L.).

AUTHOR CONTRIBUTIONS

M.Z., J.S.W., and S.R. designed the experiments. A.M.L. provided early samples of the TGIRT enzymes and advice on troubleshooting and methods. M.Z., P.G., and S.R. performed the experiments and analyzed the data with help from S.P. M.Z., J.S.W., and S.R. drafted and revised the manuscript, and all authors reviewed the manuscript and provided comments.

COMPETING FINANCIAL INTERESTS

The authors declare competing financial interests: details are available in the [online version of the paper](#).

Reprints and permissions information is available online at <http://www.nature.com/reprints/index.html>.

- Mortimer, S.A., Kidwell, M.A. & Doudna, J.A. Insights into RNA structure and function from genome-wide studies. *Nat. Rev. Genet.* **15**, 469–479 (2014).
- Deigan, K.E., Li, T.W., Mathews, D.H. & Weeks, K.M. Accurate SHAPE-directed RNA structure determination. *Proc. Natl. Acad. Sci. USA* **106**, 97–102 (2009).
- Ouyang, Z., Snyder, M.P. & Chang, H.Y. SeqFold: genome-scale reconstruction of RNA secondary structure integrating high-throughput sequencing data. *Genome Res.* **23**, 377–387 (2013).
- Rouskin, S., Zubradt, M., Washietl, S., Kellis, M. & Weissman, J.S. Genome-wide probing of RNA structure reveals active unfolding of mRNA structures *in vivo*. *Nature* **505**, 701–705 (2014).
- Wells, S.E., Hughes, J.M., Igel, A.H. & Ares, M. Jr. Use of dimethyl sulfate to probe RNA structure *in vivo*. *Methods Enzymol.* **318**, 479–493 (2000).
- Mortimer, S.A. & Weeks, K.M. A fast-acting reagent for accurate analysis of RNA secondary and tertiary structure by SHAPE chemistry. *J. Am. Chem. Soc.* **129**, 4144–4145 (2007).
- Smola, M.J., Rice, G.M., Busan, S., Siegfried, N.A. & Weeks, K.M. Selective 2'-hydroxyl acylation analyzed by primer extension and mutational profiling (SHAPE-MaP) for direct, versatile and accurate RNA structure analysis. *Nat. Protoc.* **10**, 1643–1669 (2015).
- Ding, Y. *et al.* *In vivo* genome-wide profiling of RNA secondary structure reveals novel regulatory features. *Nature* **505**, 696–700 (2014).
- Lucks, J.B. *et al.* Multiplexed RNA structure characterization with selective 2'-hydroxyl acylation analyzed by primer extension sequencing (SHAPE-Seq). *Proc. Natl. Acad. Sci. USA* **108**, 11063–11068 (2011).
- Spitale, R.C. *et al.* Structural imprints *in vivo* decode RNA regulatory mechanisms. *Nature* **519**, 486–490 (2015).
- Poulsen, L.D., Kielpinski, L.J., Salama, S.R., Krogh, A. & Vinther, J. SHAPE Selection (SHAPEs) enrich for RNA structure signal in SHAPE sequencing-based probing data. *RNA* **21**, 1042–1052 (2015).
- Kwok, C.K., Tang, Y., Assmann, S.M. & Bevilacqua, P.C. The RNA structurome: transcriptome-wide structure probing with next-generation sequencing. *Trends Biochem. Sci.* **40**, 221–232 (2015).
- Strobel, E.J., Watters, K.E., Loughrey, D. & Lucks, J.B. RNA systems biology: uniting functional discoveries and structural tools to understand global roles of RNAs. *Curr. Opin. Biotechnol.* **39**, 182–191 (2016).
- Homan, P.J. *et al.* Single-molecule correlated chemical probing of RNA. *Proc. Natl. Acad. Sci. USA* **111**, 13858–13863 (2014).
- Siegfried, N.A., Busan, S., Rice, G.M., Nelson, J.A.E. & Weeks, K.M. RNA motif discovery by SHAPE and mutational profiling (SHAPE-MaP). *Nat. Methods* **11**, 959–965 (2014).
- Smola, M.J., Calabrese, J.M. & Weeks, K.M. Detection of RNA-protein interactions in living cells with SHAPE. *Biochemistry* **54**, 6867–6875 (2015).
- Inoue, T. & Cech, T.R. Secondary structure of the circular form of the Tetrahymena rRNA intervening sequence: a technique for RNA structure analysis using chemical probes and reverse transcriptase. *Proc. Natl. Acad. Sci. USA* **82**, 648–652 (1985).
- Mohr, S. *et al.* Thermostable group II intron reverse transcriptase fusion proteins and their use in cDNA synthesis and next-generation RNA sequencing. *RNA* **19**, 958–970 (2013).
- Katibah, G.E. *et al.* Broad and adaptable RNA structure recognition by the human interferon-induced tetratricopeptide repeat protein IFIT5. *Proc. Natl. Acad. Sci. USA* **111**, 12025–12030 (2014).
- Beckman, R.A., Mildvan, A.S. & Loeb, L.A. On the fidelity of DNA replication: manganese mutagenesis *in vitro*. *Biochemistry* **24**, 5810–5817 (1985).
- Badis, G., Saveanu, C., Fromont-Racine, M. & Jacquier, A. Targeted mRNA degradation by deadenylation-independent decapping. *Mol. Cell* **15**, 5–15 (2004).
- Aviran, S. & Pachter, L. Rational experiment design for sequencing-based RNA structure mapping. *RNA* **20**, 1864–1877 (2014).

23. Hooks, K.B. & Griffiths-Jones, S. Conserved RNA structures in the non-canonical Hac1/Xbp1 intron. *RNA Biol.* **8**, 552–556 (2011).
24. Ben-Shem, A. *et al.* The structure of the eukaryotic ribosome at 3.0 Å resolution. *Science* **334**, 1524–1529 (2011).
25. Aragón, T. *et al.* Messenger RNA targeting to endoplasmic reticulum stress signaling sites. *Nature* **457**, 736–740 (2009).
26. Latrèche, L., Jean-Jean, O., Driscoll, D.M. & Chavatte, L. Novel structural determinants in human SECIS elements modulate the translational recoding of UGA as selenocysteine. *Nucleic Acids Res.* **37**, 5868–5880 (2009).
27. Chartrand, P., Meng, X.H., Singer, R.H. & Long, R.M. Structural elements required for the localization of *ASH1* mRNA and of a green fluorescent protein reporter particle *in vivo*. *Curr. Biol.* **9**, 333–338 (1999).
28. Jambor, H. *et al.* Systematic imaging reveals features and changing localization of mRNAs in *Drosophila* development. *eLife* **4**, e05003 (2015).
29. MacDonald, P.M. *bicoid* mRNA localization signal: phylogenetic conservation of function and RNA secondary structure. *Development* **110**, 161–171 (1990).
30. Bullock, S.L., Ringel, I., Ish-Horowicz, D. & Lukavsky, P.J. A'-form RNA helices are required for cytoplasmic mRNA transport in *Drosophila*. *Nat. Struct. Mol. Biol.* **17**, 703–709 (2010).
31. Jambor, H., Brunel, C. & Ephrussi, A. Dimerization of *oskar* 3' UTRs promotes hitchhiking for RNA localization in the *Drosophila* oocyte. *RNA* **17**, 2049–2057 (2011).
32. Van De Bor, V., Hartswood, E., Jones, C., Finnegan, D. & Davis, I. *gurken* and the I factor retrotransposon RNAs share common localization signals and machinery. *Dev. Cell* **9**, 51–62 (2005).
33. Fields, A.P. *et al.* A regression-based analysis of ribosome-profiling data reveals a conserved complexity to mammalian translation. *Mol. Cell* **60**, 816–827 (2015).
34. Lorenz, R. *et al.* ViennaRNA Package 2.0. *Algorithms Mol. Biol.* **6**, 26 (2011).
35. Wan, Y. *et al.* Landscape and variation of RNA secondary structure across the human transcriptome. *Nature* **505**, 706–709 (2014).
36. Meyer, M., Plass, M., Pérez-Valle, J., Eyra, E. & Vilardell, J. Deciphering 3'ss selection in the yeast genome reveals an RNA thermosensor that mediates alternative splicing. *Mol. Cell* **43**, 1033–1039 (2011).
37. Babendure, J.R., Babendure, J.L., Ding, J.-H. & Tsien, R.Y. Control of mammalian translation by mRNA structure near caps. *RNA* **12**, 851–861 (2006).
38. Kudla, G., Murray, A.W., Tollervey, D. & Plotkin, J.B. Coding-sequence determinants of gene expression in *Escherichia coli*. *Science* **324**, 255–258 (2009).
39. Carlile, T.M. *et al.* Pseudouridine profiling reveals regulated mRNA pseudouridylation in yeast and human cells. *Nature* **515**, 143–146 (2014).
40. Schwartz, S. *et al.* Transcriptome-wide mapping reveals widespread dynamic-regulated pseudouridylation of ncRNA and mRNA. *Cell* **159**, 148–162 (2014).
41. Meyer, K.D. *et al.* Comprehensive analysis of mRNA methylation reveals enrichment in 3' UTRs and near stop codons. *Cell* **149**, 1635–1646 (2012).
42. Dominissini, D. *et al.* Topology of the human and mouse m6A RNA methylomes revealed by m6A-seq. *Nature* **485**, 201–206 (2012).

ONLINE METHODS

Step-by-step protocols for target-specific and genome-wide DMS-MaPseq are available as **Supplementary Protocols 1 and 2** (and refs. 43 and 44).

Media and growth conditions. Yeast strain BY4741 was grown in YPD medium at 30 °C. Saturated cultures were diluted to OD₆₀₀ of ~0.09 and grown to a final OD₆₀₀ of 0.5–0.7 at the time of DMS treatment. HEK 293T cells were grown in DMEM medium with high glucose, supplemented with glutamine, pyruvate, nonessential amino acids, and 10% fetal bovine serum (FBS); and cells were treated with DMS at ~80% confluence.

Dimethyl sulfate (DMS) modification. For *in vivo* DMS modification in yeast, 15 ml of exponentially growing yeast was incubated with 750 µl DMS (Sigma) for 4 min at 30 °C. DMS was quenched by adding a 30 ml stop solution comprised of 30% beta-mercaptoethanol (from a 14.2 M stock) and 50% isoamyl alcohol, after which cells were quickly put on ice, collected by centrifugation at 3,500 × g at 4 °C for 4 min, and washed with 10 ml 30% BME solution. Cells were then resuspended in 0.6 ml total RNA lysis buffer (6 mM EDTA, 45 mM NaOAc pH 5.5), and total RNA was purified with hot acid phenol (Ambion) and EtOH precipitation. Ribosomal RNA was depleted using RiboZero (Epicentre), either directly after RNA extraction or postligation in the genome-wide library preparation. Denatured RNA structure samples were treated as in DMS-seq⁴. For HEK 293T cells, 15 cm⁴⁵ plates with 15 ml of media were treated with the addition of 300 µl DMS and incubation at 37 °C for 4–5 min. Media with DMS was decanted, and plates were washed twice in 30% BME (v/v). Cells were resuspended in Trizol, and RNA was isolated according to the manufacturer protocol. For *D. melanogaster* oocytes, we dissected ovaries from ~100 flies (OreR strain) in 250 µl 1× PBS. We added 250 µl DMS for 5 min at 26 °C with shaking at 500 r.p.m. To stop the reaction, we added 1 ml of 30% BME (v/v) and transferred the oocytes to a sieve, where they were washed three times in 30% BME and two times with sterile water. Finally, the ovaries were collected and resuspended in 1 ml of Trizol and 10 µl BME, and total RNA was extracted.

Library generation and genome-wide DMS-MaPseq. Sequencing libraries were prepared with a modified version of the protocol used for DMS-seq⁴. Specifically, 10 µg of DMS-treated total RNA was denatured for 2 min at 95 °C then fragmented at 95 °C for 2 min in 1× RNA Fragmentation Reagent (Zn²⁺ based, Ambion). Note that this is an increase in starting material over the 1–3 µg used in our previous DMS-seq approach (REF). The reaction was stopped with 1× Stop Solution (Ambion) and quickly placed on ice. The fragmented RNA was run on a 6% Tris Borate Urea (TBU) polyacrylamide gel for 45 min at 150 V. A blue light (Invitrogen) was used for gel imaging, and RNA fragments of 100–170 nt in size were excised, depleting small ncRNA contaminants of <100 nt (tRNAs, snoRNAs). Gel extraction was performed by crushing the purified gel piece and incubating in 300 µl 300 mM NaCl at 70 °C for 10 min with vigorous shaking. The RNA was then precipitated by adding 2 µl GlycoBlue (Invitrogen) and 3× volume (900 µl) 100% EtOH, incubating on dry ice for 20 min and spinning at 20,000 × g for 45 min at 4 °C. The samples were then resuspended in 7 µl 1× CutSmart buffer (NEB), and the 3′ phosphate

groups left after random fragmentation were resolved by adding 1.5 µl rSAP (NEB), 1 µl of SUPERase Inhibitor (Ambion), and incubating at 37 °C for 1 h. After heat inactivation of the phosphatase at 65 °C for 5 min, the samples were then directly ligated to 25 pmol of miRNA cloning linker-2 (IDT) by adding 2 µl T4 RNA ligase2, truncated K227Q (NEB), 1 µl 0.1 M DTT, 6.5 µl 50% PEG, 1 µl 10× T4 RNL2 buffer, and incubating for 2 h at 25 °C. Reactions were purified by EtOH precipitation (as above), and excess linker was degraded for 1 h at 30 °C in a 20 µl reaction of 1× RecJ buffer, 1 µl SUPERase Inhibitor, 1 µl 5′ Deadenylase (Epicentre), and 1 µl RecJ exonuclease (Epicentre). Ribosomal RNA was depleted using RiboZero (Epicentre) with a final incubation of 5 min at 40 °C, instead of 50 °C as recommended in the commercial protocol, and purified by EtOH precipitation. Reverse transcription was performed in a 10 µl volume with 1 pmol oCJ200-link2. To begin, a mixture of RNA–primer–buffer was incubated at 80 °C for 2 min to denature the template, then it was returned to ice for the addition of SUPERase Inhibitor (Ambion), DTT, dNTPs, and RT enzyme to generate the final reaction conditions. For reverse transcription using superscript II with Mn²⁺ buffer, we followed the exact published reactions conditions for mutational profiling¹⁴ (0.5 mM dNTPs, 50 mM Tris–HCl pH 8.0, 75 mM KCl, 6 mM MnCl₂, and 10 mM DTT) and allowed the reaction to proceed for 2–3 h at 42 °C with 100 U of superscript II (Invitrogen). Because TGIRT may pause at modification sites, this long incubation time facilitates readthrough of multiple modifications per RNA fragment. For the TGIRT reverse transcription, a 5 min incubation at room temperature followed the initial denaturation, and the RT reaction proceeded for 1.5 h at 57 °C with 100 U TGIRT-III enzyme (InGex) and the following reaction conditions: 1 mM dNTPs, 5 mM freshly prepared DTT (Sigma-Aldrich), 10 U SUPERase Inhibitor, 50 mM Tris–HCl pH 8.3, 75 mM KCl, and 3 mM MgCl₂. After reverse transcription, 1 µl of 5 M NaOH was added and the reaction incubated for 3 min at 95 °C to degrade the RNA, followed by EtOH precipitation and gel purification to remove excess RT primer. Finally, cDNAs were circularized using CircLigase (Epicentre), and Illumina sequencing adapters and indexes were introduced by 9–13 cycles of PCR using Phusion HF Polymerase (NEB), oNTI231, and indexing primers with TruSeq 6 bp indices. Libraries were sequenced with oNTI202 in 50 nt single-end reads on the HiSeq4000 (Illumina). See primer sequences in **Supplementary Table 1**.

Library generation and targeted DMS-MaPseq. After *in vivo* DMS treatment and total RNA extraction, 5 µg of total RNA was DNase-treated for 30 min at 37 °C in 1× TURBO DNase buffer with 1 µl TURBO DNase enzyme (Thermo Fisher Scientific). Reactions were desalted using RNA Clean & Concentrator-5 columns (Zymo Research), and rRNA was depleted using RiboZero (Epicentre) or RNase H for *D. melanogaster* and HEK 293T samples; RNase H treatment was implemented with slight modifications to the published protocol⁴⁶. For the RNase H protocol, briefly, 5 µg of total RNA was depleted of small RNA species with a Zymo RNA Clean & Concentrator-5 column, retaining RNA >200 nt per manufacturer instructions. RNase H subtraction was performed by adding 5 µg of published subtraction oligos⁴⁶ in a total volume of 30 µl in 1× hybridization buffer (200 mM NaCl, 100 mM Tris pH 7.5). The mixture was incubated at 68 °C for 1 min, and the temperature was ramped down at a rate of 1 °C/min to 45 °C. MgCl₂ was

added to a 10 mM final concentration, and 3 μ l of Hybridase ThermoStable RNase H (Epicentre) was added, followed by a 30 min incubation at 45 °C. The reaction was again purified by Zymo RNA Clean & Concentrator-5 column to deplete small RNA species, followed by treatment with DNaseI (Ambion) per manufacturer instructions and a final column clean up to remove excess RNase H subtraction oligos.

20–100 ng of RNA was used for reverse transcription with 100 U TGIRT-III (InGex) for 2 h at 57 °C in the same TGIRT reaction conditions as those described above. We used 5–10 pmol of each gene-specific RT primer and successfully pooled up to six different RT primers in one reaction, using no more than 35 pmol total. DTT was prepared from powder directly before reverse transcription, and we omitted the denaturation step before reverse transcription on account of low-level fragmentation of DMS-treated RNA at high temperatures. After moving the reaction to ice, 1 μ l RNase H (Enzymatics, 5 U/ μ l) was added, and RNA–DNA hybrids were degraded at 37 °C for 20 min to release the cDNA. We used RNase H at this step for convenience—NaOH hydrolysis as used in the genome-wide protocol also works well at this step. cDNA was purified using the ssDNA protocol for DNA Clean & Concentrator-5 columns (Zymo Research). We used the Advantage HF 2 PCR kit (Clontech) with high-fidelity conditions for two-step PCR amplification, using 1/12 of the purified RT reaction and gene-specific primers targeting a single template with a target amplicon size of 300–600 nt for low-abundance RNA targets. When possible, we designed our gene-specific RT primers close to the PCR amplicon of interest, and in many cases we used the RT primer as the reverse primer in our PCR reactions. High-abundance RNAs, such as the yeast 18S rRNA, can be amplified in a single 1.8 kb amplicon. Because of the high GC content of the *FXR2* template, we used 200 mM NaCl instead of 75 mM KCl in the RT reaction buffer and the Advantage GC 2 PCR Kit (Clontech) for its amplification. The PCR program begins with 10 cycles at a 65 °C annealing temperature to promote specificity, followed by 20–25 cycles at a 57 °C annealing temperature. PCR bands were gel purified on a non-denaturing 8% TBE polyacrylamide gel (Invitrogen) and crushed, extracted, and EtOH precipitated as described above. NexteraXT (Illumina) was used to fragment and prepare amplicons (1 ng) for sequencing. Tagmented amplicons were barcoded and amplified using 12 cycles of PCR, and barcoded libraries were cleaned using 1.5 \times (v/v) PCRclean beads (Aline Biosciences). Libraries were quantified using the Fragment Analyzer (Advanced Analytical) and subjected to a final quantification by qPCR before sequencing by 50 bp single-end reads on the HiSeq4000 (Illumina).

For the UMI-based RT–PCR, reverse transcriptase primers were designed with a random 10 nt barcode, labeling each cDNA with a unique molecular index. Gene-specific variations of oMZ282 were used in the reverse transcription reaction described above, followed by Advantage HF 2 PCR with gene-specific variants of primers oMZ282 and oMZ283. Amplicons were purified by polyacrylamide gel and extracted as described above, and a second round of PCR was done with 20–25 cycles to add Illumina adaptors and indices for sequencing (oMZ284 and indexing primers). Libraries were constructed so the UMI was sequenced first using custom Read1 sequencing primer oNTI202. We used the standard Illumina Read2 primer, and sequencing was done via MiSeq v2 2 \times 150 (Illumina). See primer sequences in **Supplementary Table 1**.

Ribosnitch RNA preparation. dsDNA corresponding to the human *MRPS21* sequences shown below were *in vitro* transcribed, mixed, and folded by denaturing at 95 °C followed by a brief incubation at 37 °C in 350 mM sodium cacodylate buffer and 6 mM MgCl₂. 10% DMS (v/v) was added, and the sample was incubated for 10 min at 37 °C. The reaction was stopped by placing on ice and adding BME to 30% final volume. The RNA was then purified by RNA Clean & Concentrator-5 column (Zymo), and the small RNA fraction was collected and prepared for sequencing as described in the genome-wide strategy above.

MRPS21 A allele: 5'-TGCTGCCATCTCTTTTCTTCTCTATGCGAGGATTTGGACTGGCAGTG-3'; *MRPS21* C allele: 5'-ATCTCTTTTCTTCTCTCTGCGAGGATTTGGACTGGCAGTGAG AATAAGAGACAA-3'.

Sequencing alignment and analysis. Raw fastq files were stripped of linker sequences and filtered for quality using the FASTX-Toolkit Clipper and Quality Filter functions, respectively, requiring that 80% of sequenced bases have a quality score >25 (http://hannonlab.cshl.edu/fastx_toolkit/). Reads were aligned using Tophat v2.1.0 with bowtie2 with the following settings for a 50 nt sequencing run: –no-novel-juncs -N 5 –read-gap-length 7 –read-edit-dist 7 –max-insertion-length 5 –max-deletion-length 5 -g 3. All nonuniquely aligned reads were then removed. Sequencing data was aligned against the *Saccharomyces cerevisiae* assembly R64 (UCSC, sacCer3) downloaded from the *Saccharomyces* Genome Database on February 8, 2011 (SGD, <http://www.yeastgenome.org>) or against the longest human RefSeq isoforms (hg19). Despite template-switching capabilities of the TGIRT enzyme, we did not detect a substantial number of chimeric reads in our data and did not include a processing step beyond alignment to remove these. On account of empirically determined mutation enrichment from nontemplate addition and Nextera XT transposase insertion, we trimmed 2, 5, and 7 nt from the 5' end of each read for TGIRT-, SSII–Mn²⁺-, and NexteraXT-generated libraries, respectively. Mismatches located within 3 nt of an indel were also discarded for future analysis. The ratiometric DMS signal was calculated for each nucleotide as number of mismatches/sequencing depth.

Target-specific sequencing data prepared with NexteraXT were combined across both strand alignments, because of lack of strandedness after tagmentation. Transposase insertion is subject to primary sequence biases in transposase insertion; thus it is possible (although rare) to have amplicon regions that are poorly sampled and result in false-positive bases with high ratiometric reactivity due to poor sequencing depth. After linker stripping with a length requirement for reads >100 nt from a 2 \times 150 nt MiSeq run, target-specific sequencing data prepared with the UMI was collapsed to unique reads using FASTX-Collapser. Unique reads are, therefore, the combination of a unique molecular index and internal DMS-induced modifications, which add sequence diversity beyond the 10 bp UMI.

Genome-wide yeast DMS–MaPseq data was collected and sequenced with two biological replicates for each SSII–Mn²⁺ and TGIRT, untreated and *in vivo* DMS-treated libraries. For each library variation, we collected a combined total of 90 to 200 million uniquely mapped reads between yeast replicates and 200 million for HEK 293T cells. Note that we sequenced to a similar depth for a genome-wide DMS–MaPseq experiment as we did for our previously published genome-wide DMS-seq method⁴³.

HEK 293T Gini index calculations. UTR and coding regions were defined by RefSeq coordinates, and we analyzed 50 nt windows beginning at the annotated transcription start site. After requiring a minimum number of 100 total reads at As or Cs and >20× mismatch coverage for each window, we also discarded any windows with evidence for endogenous modifications (>15% mismatch rate). The Gini index was calculated only for A and C bases, as done previously⁴.

Minimum average coverage calculation. Using 100 nt transcriptome windows, we chose the window with the highest total sequence coverage as representative coverage for the gene. We counted the fraction of genes from the hg19 RefSeq annotation that had an average mismatch coverage >120 mismatches at sequencing depths of 50, 100, and 200 million uniquely mapped reads. We extrapolated the data for 1 billion reads.

Computing the ROC curve for ribosomal RNA. This analysis was completed as previously described, using the yeast ribosome crystal structure²⁴ and the same considerations for solvent accessibility and removal of outliers by 90% Winsorization⁴.

Secondary structure models. Novel secondary structure models were generated using constraints derived from DMS-MaPseq data using RNAfold³⁴. For *FXR2*, the sequence corresponding to nucleotides 1–450, which comprise the 5′ UTR and first exon, were folded in RNAfold. Adenine and cytosine bases with an *in vitro* ratiometric signal greater than the selected threshold (which varied between 0.03 and 0.06, as specified in the relevant figure legends) were required to be unpaired. Depending on the threshold used, small differences exist in the predicted structure; however, the 0.04 constraint threshold appears to produce the best fitting model for our experimental data. Because of the high GC content of the *FXR2* region (80% GC) and the necessity of using a low-fidelity GC polymerase for these experiments, an untreated control was used to mask ten positions with reactivity above background. DMS-MaPseq reactivities were overlaid on structure models using VARNA (<http://varna.lri.fr/>)⁴⁷.

Cloning and transfection experiments. The plasmid construct in **Supplementary Figure 5** was derived from the Δ ATG *FXR2* exon1–eGFP–IRES–mCherry plasmid described in Fields *et al.*³³.

A gBlock (IDT) was ordered containing a 43bp *FXR2*–3×FLAG–T2A–AgeI–eGFP (40-bp fragment) for HiFi assembly (NEB) into the linearized plasmid backbone. This wild-type plasmid was used as the PCR template for *FXR2* mutations, which were designed as overhangs on primers against the relevant portion of the *FXR2* exon1 sequence, resulting in 5′ and 3′ fragments with overlapping mutated regions for HiFi assembly into the linearized wild-type backbone. Successful amplification of fragments was confirmed by running a fraction on an agarose gel, and the remainder of the fragments was purified using DNA Clean & Concentrator-5 columns (Zymo) or, in the case of contaminating PCR bands, purified via agarose gel and MinElute gel extraction (Qiagen). Common cloning primers for *FXR2* amplification from the plasmid are 5′-CTCACTCGGCGCGCCAGTC-3′ (5′ *FXR2* fragment, forward) and 5′-TATAGTCCCCGTCGTGATCCTTGTA-3′ (3′ *FXR2* fragment, reverse). Inserts in all analyzed constructs were confirmed by Sanger sequencing (Molecular Cloning Laboratories). Plasmids are listed in **Supplementary Table 2**.

For fluorescence measurements, HEK 293T cells were grown as described and transfected with plasmids using TransIT-LT1 (Mirus) 2 d before data collection. eGFP and mCherry fluorescence were quantified using an LSR-II flow cytometer (BD Biosciences). Two plasmids for each type of mutation were assayed for fluorescence, serving as biological duplicates.

Code availability. Our code is publically available at <https://github.com/spersad94/DMS-MaP-Seq-Code>.

Cell lines. HEK 293T cells were obtained from ATCC.

43. Zubrardt, M. *et al.* Genome-wide DMS-MaPseq for *in vivo* RNA structure determination. *Protocol Exchange* <http://dx.doi.org/10.1038/protex.2016.068> (2016).
44. Zubrardt, M. *et al.* Target-specific DMS-MaPseq for *in vivo* RNA structure determination. *Protocol Exchange* <http://dx.doi.org/10.1038/protex.2016.069> (2016).
45. Ingolia, N.T., Ghaemmaghami, S., Newman, J.R.S. & Weissman, J.S. Genome-wide analysis *in vivo* of translation with nucleotide resolution using ribosome profiling. *Science* **324**, 218–223 (2009).
46. Adiconis, X. *et al.* Comparative analysis of RNA sequencing methods for degraded or low-input samples. *Nat. Methods* **10**, 623–629 (2013).
47. Darty, K., Denise, A. & Ponty, Y. VARNA: interactive drawing and editing of the RNA secondary structure. *Bioinformatics* **25**, 1974–1975 (2009).